High Temperature Corrosion of Materials (2023) 100:321–344
https://doi.org/10.1007/s11085-023-10182-2

ORIGINAL PAPER

Comparative Study of FeCrAlY and Sapphire Hot Corrosion by Mixed Oxide and Sulfate Deposits

Atharva S. Chikhalikar[1] · **David L. Poerschke**[1]

Received: 24 April 2023 / Revised: 3 August 2023 / Accepted: 5 August 2023 /

Abstract

Alloys and oxidation-resistant coatings utilized in high-temperature applications can be degraded by aerosols that deposit onto surfaces during operation. Understanding how the deposit composition influences the hot corrosion mechanisms is essential to develop more durable materials. This work advances the understanding of the effect of complex oxide and sulfate deposits on the degradation of an alumina-forming FeCrAlY alloy in comparison to reactions with single-crystal sapphire. The deposit compositions were developed to systematically understand the effect of anion makeup (mixed oxides, oxide–sulfate, and sulfates) and the effect of adding Na and K salts. $CaSO_4$ was used as a control. The mixed oxide and oxide–sulfate deposits increased the frequency of thermally grown oxide (TGO) intrusions in FeCrAlY but did not produce a noticeable change in the sapphire. Pure $CaSO_4$ and mixed sulfate reacted with the TGO and sapphire to form calcium aluminates and led to roughening of the specimen–reaction product interface. The primary difference between the $CaSO_4$ and mixed sulfate deposits was the increased uniformity of the attack by the latter due to its tendency to melt and spread. Comparison between the change in the degradation features in the presence of $CaSO_4$ and mixed sulfate deposits on both types of specimens expands the current understanding of sulfate-based hot corrosion.

Keywords High-temperature corrosion · Oxide–sulfate deposits · Sapphire · FeCrAlY alloy · Energy dispersive x-ray spectroscopy

---

✉ David L. Poerschke
dpoersch@umn.edu

[1] Department of Chemical Engineering and Material Science, University of Minnesota, Minneapolis, USA

Introduction

Hot-section components in aviation, marine, and land-based power generation turbines are made from alloys that need to withstand mechanical stresses and oxidation under thermal cycling. Oxidation resistance is achieved by forming a passivating thermally grown oxide (TGO) on the alloy or on an oxidation-resistant metallic coating [1, 2]. Unfortunately, deposits formed from aerosol debris can attack the TGO, accelerating degradation via various high-temperature corrosion mechanisms. Recent reports show that in addition to the well-documented corrosion by Na_2SO_4-based deposits [3–11], deposit-induced degradation of alumina-forming alloys also occurs at higher temperatures in the presence of CaO- and $CaSO_4$-containing deposits that convert the TGO into less-protective calcium aluminates and chromates and can drive alloy sulfidation [12–17]. The examination of ex-service turbine components and complementary laboratory experiments indicates that complex deposits (such as multi-cation sulfate, sulfate-oxide, and sulfate-oxide-chloride chemistries) accelerate oxidation over a range of temperatures via varying mechanisms [14, 16, 18–24]. The cation stoichiometries in these complex deposits often resemble the CMAS or CMFAS deposits that accelerate the failure of thermal and environmental barrier coatings at higher temperatures in turbine environments [24–28].

Understanding how temperature and the composition of the alloy, TGO, deposit, and atmosphere influence the hot corrosion mechanism and severity is critical to accelerating the development of new corrosion-resistant alloys. Recent work toward this objective has demonstrated that sulfates in mixed oxide–sulfate deposits decompose more readily than pure sulfates due to favorable reactions with oxides to form aluminosilicates [29]. At the same time, the transient presence of Na_2SO_4 reduces the incipient melting temperature of the mixed oxide–sulfate deposits, increasing the tendency for the deposit to spread relative to the location where the material was initially deposited. Related work applied image analysis to quantify the features relevant to understand alloy degradation by these complex deposits [17]. Those results showed that a multi-cation oxide deposit produced only occasional localized attack in the form of TGO intrusions into the alloy, while a comparable multi-cation sulfate deposit caused a more significant and uniform attack across the alloy. In the latter case, the fluxing effect of Na_2SO_4 in the mixed sulfate deposit facilitated deposit spreading, but the underlying TGO-attack mechanism forming calcium aluminates was similar to pure $CaSO_4$ [16, 17, 30]. Given the complexity of deposit compositions and the variety of degradation mechanisms, high throughput screening protocols are needed to accelerate efforts to understand the mechanisms. Toward this objective, this study addresses the following questions:

- To what extent does the transient presence of volatile, low-melting Na and K oxides and sulfates change the deposit-induced corrosion pathway?
- What differentiates the behavior of multi-cation oxide vs. multi-cation oxide–sulfate deposits, considering the fast intrinsic decomposition of sulfates in such deposits?

- How do the dynamics of finite TGO consumption, alloy re-passivation, and alloy defects influence the corrosion process, compared to deposit reactions with a semi-infinite alumina substrate?

The approach decouples these effects by comparing the consequence of systematic changes in the deposit composition on reactions with a model Al_2O_3-forming FeCrAlY alloy and single-crystal sapphire. Using image analysis to quantify features including the reaction product thickness and the alloy/TGO interface roughness, the work generates datasets to feed future data-driven materials discovery efforts, while also extending the fundamental understanding of the variables influencing the deposit-induced degradation behavior.

Experimental Procedures

Deposit Selection and Preparation

Six model deposits (Table 1) were selected to systematically compare the role of the anion makeup (just oxides, just sulfates, or mixtures of oxides and sulfates) and the presence or absence of Na and K salts. These compositions are based on a master cation stoichiometry $C_{13}N_{10}K_1M_{11}F_{11}A_{14}S_{40}$, which was defined in prior work based on additions of Mg, Fe, Al, Na, K to a commonly studied, moderate Ca/Si ratio CMFAS oxide composition [17, 29, 31, 32]. The CMFAS and CNMKFAS variants study the effect of Na and K, which are known to depress the melting point of the corresponding oxide and sulfate mixtures [29][40, 41]. The –O and –O$\overline{S}$ variants compare the behavior of deposits based on oxides (–O) relative to an oxide–sulfate

Table 1 Summary of deposit compositions (mol %)*

ID & Cation Stoichiometry	$C_{15}M_{12}F_{12}A_{16}S_{45}$		$C_{13}N_{10}K_1M_{11}F_{11}A_{14}S_{40}$		$C_{37}N_{28}K_3M_{31}$	C_{100}
↓ Component	CMFAS-O	CMFAS-$O\overline{S}$	CNKMFAS-O	CNKMFAS-$O\overline{S}$	CNKM-$\overline{S}$	$CaSO_4$
$AlO_{1.5}$	16	16	14	14	–	–
CaO	15	10	13	9	–	–
$FeO_{1.5}$	12	12	11	11	–	–
$KO_{0.5}$	–	–	1	0.7	–	–
MgO	12	8	11	7	–	–
$NaO_{0.5}$	–	–	10	7	–	–
SiO_2	45	45	40	40	–	–
$CaSO_4$	–	5	–	5	37	100
$K(SO_4)_{0.5}$	–	–	–	0.3	3	–
$MgSO_4$	–	4	–	4	28	–
$Na(SO_4)_{0.5}$	–	–	–	3	31	–

*Single cation cement chemistry notation C = CaO, A = $AlO_{1.5}$, S = SiO_2, $\overline{S}$ = SO_3 etc.

mixture ($-\mathrm{O}\overline{\mathrm{S}}$) formulated with Ca, Mg, Na, and K added in a 1:2 sulfate-to-oxide ratio. Other cations including Fe, Al, and Si were added only as oxides based on the relative instability of the silicon, iron, and aluminum sulfates relative to their oxides [33–35]. The mixed sulfate $\mathrm{CNMK}-\overline{\mathrm{S}}$ deposit maintains the relative Ca, Mg, Na, and K ratios of $\mathrm{CNKMFAS}-\mathrm{O}$ using just sulfates. Pure anhydrous $CaSO_4$ was used for comparison to other studies.

The model deposits were synthesized from the individual components procured from Alfa Aesar (AA, Ward Hill, MA) or Acros Organics (AO, Morris Hill, NJ). CaO (99.95% pure, AA), MgO (98%, AO), Fe_2O_3 (99.9%, AA), Al_2O_3 (99.95%, AA), and SiO_2 (99%, AA) were utilized as the CMFAS oxide sources. Sodium aluminate (tech. grade, AA) and potassium silicate (2.5:1 wt.% SiO_2/K_2O, AA) were used as sources for Na_2O and K_2O, respectively (with corresponding adjustments to the total SiO_2 and Al_2O_3 added), since these compounds are more stable and easier to work with during processing than pure Na_2O and K_2O. $CaSO_4$ (99%, AO), $MgSO_4$ (99.5%, AA), Na_2SO_4 (99%, AO), and K_2SO_4 (99 + %, AO) were used as the sources for sulfates. To produce well-mixed, pre-reacted crystalline powders, the individual chemicals were mixed and taken through sequential dehydration, calcining, ball milling, drying and pre-reaction steps. Alumina milling media with ethanol as the dispersing agent was utilized for ball milling. The pre-reaction temperature for these mixed deposits was determined to prevent incipient melting of the deposit or sulfate decomposition prior to the hot corrosion experiments. Additional details of the deposit preparation procedure are provided elsewhere [29].

Oxidation Testing

Tests were conducted on two substrate types. Oblong disks 12 mm long, 8 mm wide, and 2 mm thick were cut from an alloy rod of nominal composition (wt.%) Fe-22Cr-5Al-0.1Y-0.1Zr (FeCrAlY, Goodfellow Corporation, Coraopolis, PA). Polished sapphire single crystals (α-Al_2O_3, Advalue Technology, Tucson, AZ) were cut into rectangular specimens approximately 12 mm by 8 mm. The FeCrAlY specimens were polished using SiC abrasive papers and diamond polishing liquid to a 1 µm finish. The specimens were ultrasonically cleaned sequentially in a 2 wt.% microorganic soap solution, 200 proof ethanol, and acetone. The specimen dimensions and mass were measured before and after each subsequent step. The FeCrAlY specimens were pre-oxidized for 100 h in dry air (<6 ppm H_2O, 0.2 l/min, 30 mm OD fused quartz furnace tube) at 1025 °C (10 °C/min heating, 8 °C/min maximum cooling rate), generating a uniform α-Al_2O_3 TGO.

The deposit powders were applied using a stencil to achieve a ~ 25 mg/cm^2 loading over a 4 mm diameter circle. The specimens were placed in alumina boats (Coorstek Inc., Golden, CO) and annealed for 100 h at 1025 °C in dry air using the same conditions as the pre-oxidation. Because initial experiments exposing FeCrAlY to each of the six deposits showed minimal reaction between the $\mathrm{CMFAS}-\mathrm{O}$ and $\mathrm{CMFAS}-\mathrm{O}\overline{\mathrm{S}}$ deposits and the alumina TGO, these deposits were not tested on sapphire. To prevent cross-contamination, separate furnace tubes and boats were utilized for each deposit type.

Two separate experiments were performed to establish the baseline behavior in the absence of deposits. In the first experiment, a single pre-oxidized FeCrAlY specimen was further oxidized at 1025 °C for 100 h in the center of the alumina boat and at the center of the furnace hot zone without a surface deposit. The second experiment (modified baseline) sought to account for (i) the presence of multiple specimens in the boat, (ii) slight deviations from the center of the hot zone (but within ± 10 °C of the target temperature), and (iii) changes in gas flow across the specimen due to the solid deposit. Three FeCrAlY specimens were pre-oxidized for 100 h in dry air at 1025 °C in the same boat. The center specimen was centered in the hot zone, and the other two specimens were positioned on each side of the center specimen. The three specimens were then oxidized for an additional 100 h in dry air at 1025 °C in the same boat, but with 4 mm diameter, 2.5 mm tall cylinders cut from a four-bore alumina tube placed on each specimen to simulate the presence of a deposit. The sapphire baseline specimen was heat-treated at 1025 °C for 100 h without a surface deposit according to the first FeCrAlY baseline experiment format.

Characterization

The annealed specimens were inspected to determine the degree of deposit adherence, melting, and spreading. Photo-stimulated luminescence spectroscopy (PSLS) measured using a 532 nm Nd:YAG laser on the Witec Alpha 300R Raman microscope was used to confirm the presence of α-Al_2O_3 in the TGO. Polished cross sections were characterized by scanning electron microscopy (SEM, Hitachi SU8230) and energy-dispersive X-ray spectroscopy (EDS, Thermo-Noran Vantage on a JEOL JSM 6500 SEM). To prevent the loss of water-soluble species in the residual deposits and reaction products, the cutting, grinding, and polishing employed water-free lubricants. Backscattered electron (BSE) micrographs were recorded across the entire cross section at a sufficiently high magnification to identify details of the TGO and TGO-alloy interface. These images were stitched together and analyzed to quantify (i) the thickness of the TGO and reaction product (TGO + RP) layer and (ii) the local variation in the TGO-alloy or reaction product/sapphire interface using a previously-reported method [17].

Results and Discussion

This section first discusses the general observations regarding the appearance of the specimens and the surface characterization. Then the reaction mechanisms for each deposit type are discussed. Finally, data from image analysis are used to discuss the prevalence and statistical variation in important degradation features.

General Observation and Surface Characterization

All deposits except the mixed sulfates, which melted and spread, shrank but otherwise remained solid and adhered to the specimen surfaces. The implication is that

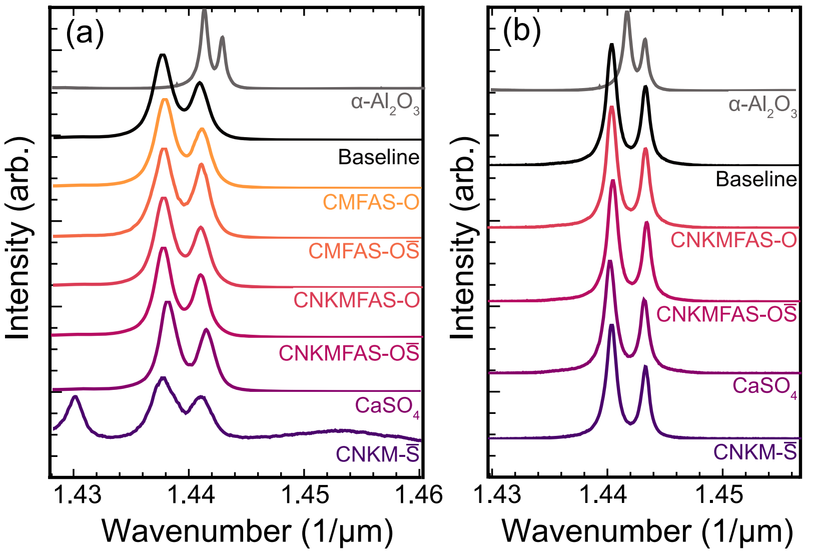

Fig. 1 PSLS spectra for the **a** FeCrAlY and **b** sapphire specimens after deposit degradation experiments, compared to an α-Al$_2$O$_3$ powder standard

any melt in those deposits is a sufficiently small fraction to not coalesce the powder. The surface of the sapphire was more opaque in a region extending ~ 1 mm away from the deposits, although subsequent characterization showed no significant structural or chemical change. PSLS spectra taken away from the initial deposit location (Fig. 1a and b for the FeCrAlY alloy and sapphire specimens respectively) show the characteristic doublet peaks for α-Al$_2$O$_3$. The shift in the peak positions recorded for the alloy relative to the α-Al$_2$O$_3$ powder standard is due to the residual growth stresses in the TGO [36, 37]. The additional peaks in the spectra for the FeCrAlY specimen exposed to the CNKM − $\overline{S}$ deposit are believed to originate from the residual deposit layer.

Influence of Deposit Composition on Local Reactions

Reactions with CaSO$_4$

Figure 2 shows cross section BSE micrographs and EDS maps of the specimens exposed to CaSO$_4$. Regions outside the initial deposit location showed no evidence of reaction products except those due to occasional CaSO$_4$ particles scattered during handling or by the airflow. Under the deposits, Al$_2$O$_3$ reacted with CaSO$_4$ forming a mixture of calcium aluminates. The top of this layer contained sulfur, suggesting that some residual CaSO$_4$ is embedded in the reaction product layer. Based on semi-quantitative measurements of the Ca/Al ratio, the alloys forms two distinct layers containing mixtures of calcium aluminates, abbreviated C$_x$A$_y$. The average Ca/Al ratios measured by EDS and comparisons with prior reports [13, 38, 39] suggest that

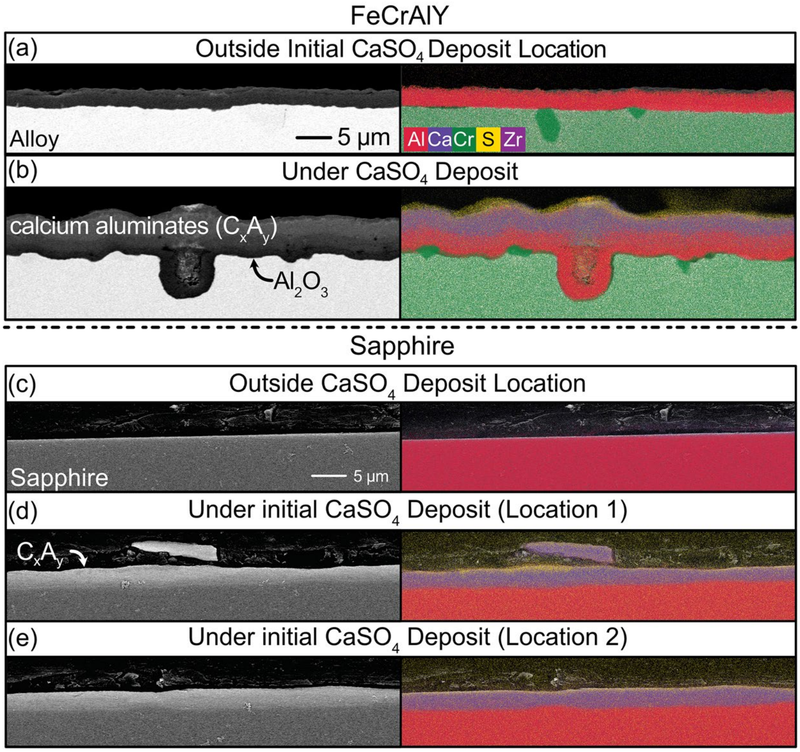

Fig. 2 Corrosion products formed on the **a**, **b** FeCrAlY alloy (adapted from [17]) and **c**–**e** sapphire exposed to $CaSO_4$. The left column shows BSE images, and the right column shows EDS maps of key elements

the outer C_xA_y layer consists of Ca-rich $Ca_3Al_2O_6$ (C_3A) and $C_{12}Al_{14}O_{33}$ ($C_{12}A_7$) and the inner C_xA_y layer is primarily the Ca-lean $CaAl_2O_4$ (CA). A uniform Al_2O_3 layer was present at the alloy-TGO interface (see Fig. 2b). The reactions with sapphire produced three distinct layers. The top layer consisted of a mixture of $C_{12}Al_{14}O_{33}$ ($C_{12}A_7$) and $CaAl_2O_4$ (CA). The second layer is comprised mainly of $CaAl_2O_4$. Finally, the layer adjacent to the sapphire consisted of a mixture of $CaAl_2O_4$ and Ca-lean $CaAl_4O_7$ (CA_2) (see Fig. 2d,e).

The solid-state nature of the deposit and the through-thickness reduction in Ca concentration through the reaction layer thickness suggests that the reactions involved diffusion of Ca toward the alloy. The C_xA_y formation increases the overall TGO + RP thickness in the region under the initial deposit. As elaborated later, the RP thickness varies throughout the region under the $CaSO_4$ deposit for both specimens. This is attributed to the inconsistent contact between the solid (powdered) deposit and the specimen.

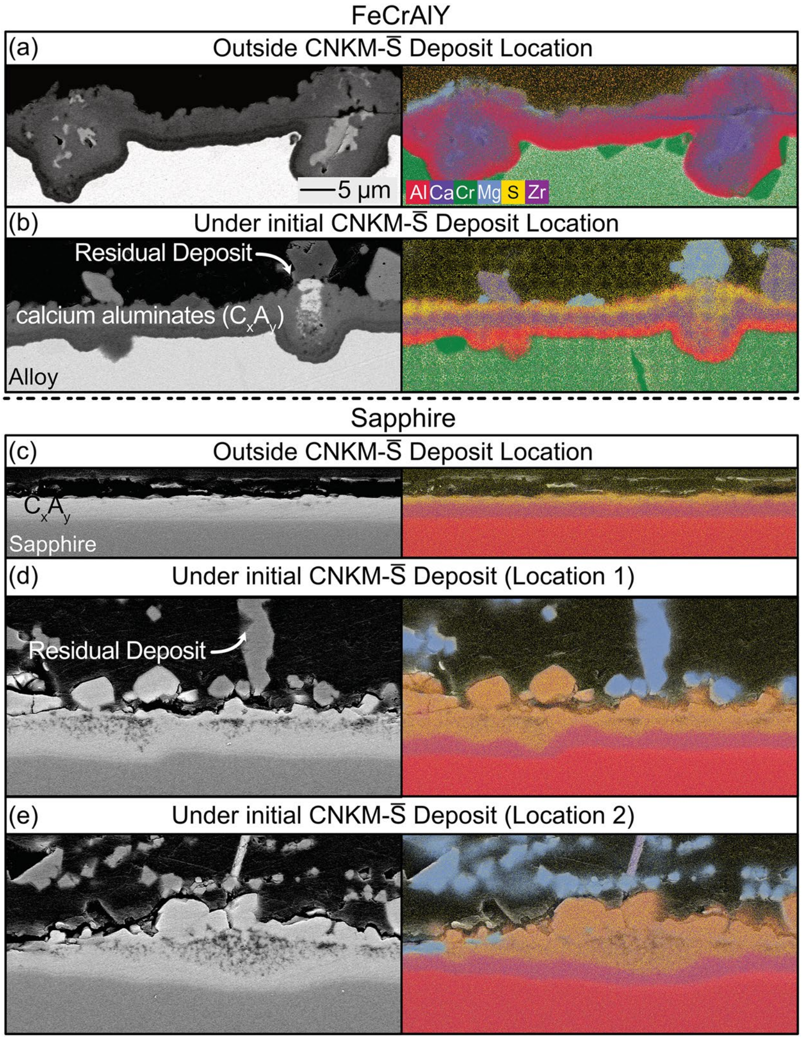

Fig. 3 Analysis of the corrosion products formed on the **a**, **b** FeCrAlY alloy (adapted from [17]) and **c**–**e** sapphire exposed to $\mathrm{CNKM}-\overline{\mathrm{S}}$. The left column shows BSE images, and the right column shows EDS maps of key elements

Reactions with $CNKM-\overline{S}$

Figure 3 shows representative cross sections of the specimens exposed to $\mathrm{CNKM}-\overline{\mathrm{S}}$. Because the deposit melted and spread, both specimens were affected well away from the initial deposit location. As with pure $CaSO_4$, calcium aluminates (with some intermixed $CaSO_4$) are the predominant reaction products. On the alloy, the layer below the S-containing surface layer comprises a mixture of $C_{12}A_7$

and CA, followed by a thin layer of Ca-lean CA and then α-Al_2O_3 adjacent to the alloy. The composition of reaction products varied on the sapphire moving from under to outside the initial deposit location. Under the initial deposit, the top layer consisted of residual $CaSO_4$ with a mixture of porous C_xA_y products with an inner layer comprising a mixture of Al-rich aluminates (CA and CA_2). Outside the initial deposit, the entire reaction layer was dense with a thin $CaSO_4$ layer on top of mixed Al-rich aluminates. Undulations were observed at the interface between the reaction product layers and both substrates. The alloy specimen showed periodic deeper oxide intrusions into the alloy, but limited cracking or delamination. Conversely, no significant intrusions were observed in the sapphire substrate but there was more significant cracking and delamination of the reaction products. It is unclear whether the increased cracking in the sapphire specimen was due to differences in the thermochemical/mechanical interactions during the test, or if this is an artifact of the post-test specimen preparation. Discrete MgO particles were adhered to the top of the calcium aluminate reaction layer. These appear predominantly in the region under the initial deposit (see Fig. 3b,d,e). Occasional small Mg-rich inclusions were observed toward the periphery. There was no evidence that the MgO reacted with the alumina. Na and K were not observed in the reaction products or in the remaining deposit.

The observations can be explained by the following reaction sequence. The Na_2SO_4 depresses the melting point of the $\mathrm{CNKM}-\overline{\mathrm{S}}$ deposit. Mixtures of $MgSO_4$ and Na_2SO_4 melt around 700 °C and can dissolve ~ 10 mol.% $CaSO_4$, the $CaSO_4$-Na_2SO_4 eutectic is around 900 ℃, and by 1000 °C 50 mol.% $CaSO_4$ can dissolve in the ternary melt [40, 41]. Given its relative instability, the $MgSO_4$ begins to decompose during this process leaving MgO particles and a reduced fraction of $MgSO_4$ in the melt [29, 42]. This melt spreads over the surface, dissolving Al_2O_3 from the TGO or sapphire substrate, and precipitating calcium aluminates. Na_2SO_4 volatilization leaves a solid mixture of $CaSO_4$ and aluminates that continue reacting for the remainder of the heat treatment.

The primary difference between the FeCrAlY and sapphire specimens is the thicker, more porous reaction layer under the initial deposit on sapphire. Several, potentially concurrent, reaction mechanisms are plausible. The first is that the initial, highly reactive melt rapidly dissolves the semi-infinite sapphire, while the dissolution of the FeCrAlY TGO is limited by the finite Al_2O_3 thickness. This would produce a thicker initial layer of mixed melt and calcium aluminates in the center of the sapphire specimen, which becomes a porous solid layer as the Na_2SO_4 evaporates. An alternative explanation is that subtle differences in the TGO chemistry compared to sapphire, e.g., the presence of Cr or Fe oxides from the initial transient oxidation, could alter the initial sulfate melting, spreading, and evaporation process leading to a more uniform reaction across the specimen.

Reactions with Mixed Oxide Deposits

Figure 4 shows representative cross sections of the specimens exposed to the mixed oxide deposits. The FeCrAlY specimens exhibited a uniform, adherent α-Al_2O_3

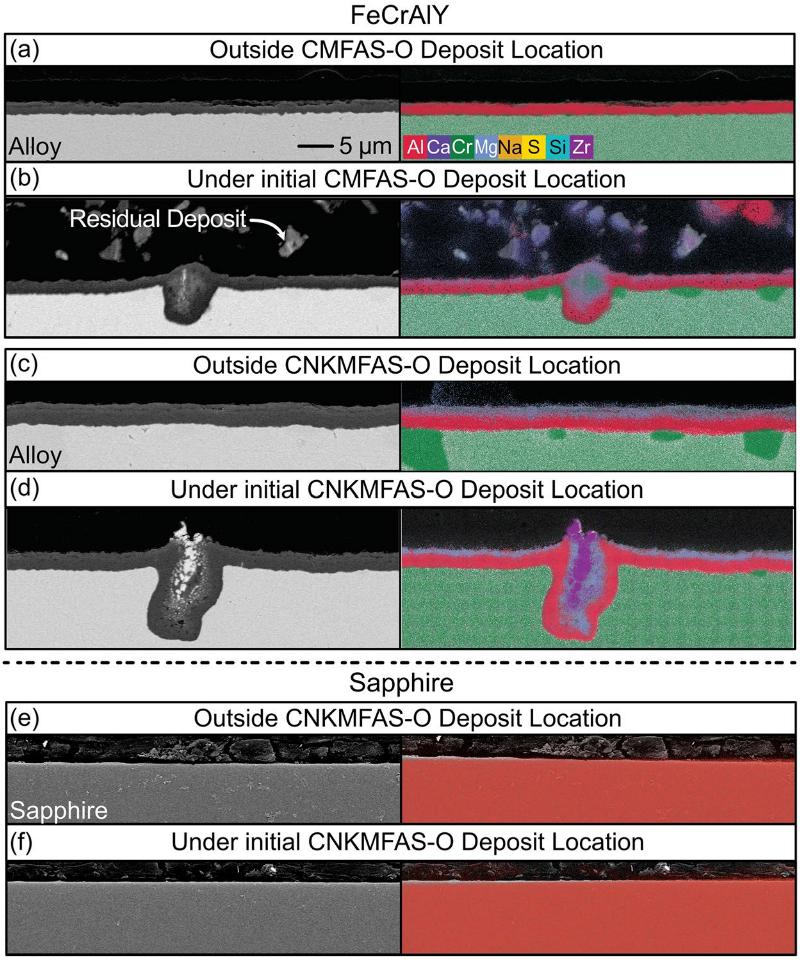

Fig. 4 Analysis of the corrosion products formed on the FeCrAlY alloy exposed to **a**, **b** CMFAS-O and **c**, **d** CNKMFAS-O deposits and on the sapphire specimen exposed to **e**, **f** CNKMFAS-O deposit. The left column shows BSE images, and the right column shows EDS maps of key elements

TGO with occasional oxide intrusions in the alloy. The primary difference between the CMFAS – O and CNKMFAS – O deposits is that the latter had an increased frequency of intrusions under the initial deposit location. Similar behavior was observed by Gheno and Gleeson [23] on NiCoCrAlY coupons exposed to mixed oxide (fly ash) deposit. The EDS analysis revealed the presence of Mg, Y, and Zr oxides in the local oxide intrusions, and a thin Mg-containing layer at the surface across the TGO. These observations are consistent with prior reports, showing that even trace Mg impurities in the alloy can produce MgO incorporation into the TGO, and that the Y and Zr oxides originate as reactive elements or impurities in the alloy [43–45]. Our collective evidence from studies on various alloys and other substrates further supports the conclusion that these species originate from within the FeCrAlY. In contrast, no intrusions or other reaction products were observed in the sapphire specimens exposed to the CNKMFAS − O deposit (Fig. 4e, f). These observations suggest that the behavior of the FeCrAlY specimens could be due to favorable contact with the deposit and features of the alloy microstructure. However, additional studies are required to identify the mechanism leading to the increased formation of intrusions.

Reactions with Mixed Oxide–Sulfate Deposits

Figure 5 shows the typical behavior of the specimens exposed to the oxide–sulfate deposits. The general characteristics were similar to the specimens exposed to the mixed oxide deposits, including a uniform and adhered TGO except for an increased presence of local oxide intrusions under the deposit. However, the CNKMFAS − OS deposit produced more adherent Na, Mg, and Ca-silicate particles in the residual deposit (see Fig. 5d). A likely explanation is the formation of a Na-rich melt during the initial heating and reduced Na volatilization due to its stabilization in mixed silicates. Similar to the CNKMFAS − O deposit [17], oxide intrusions in the alloy were composed of Mg-rich products as well as bright Y-Al-O and Zr-Al-O phases. Sulfur was not observed in the deposit or the reaction products (see Fig. 5d). No reaction products were observed on the sapphire substrate exposed to CNKMFAS − OS (see Fig. 5e,f). One explanation for the similarity between the mixed oxide and oxide–sulfate deposits is that the presence of SiO_2, Al_2O_3, and Fe_2O_3 accelerates sulfate decomposition [29], converting the sulfates to oxides early in the heat treatment.

Quantitative Analysis of Degradation Features

Variation in the Baseline Behavior

Figure 6 shows the TGO thickness as a function of specimen location for the baseline specimens described in Sect. "Oxidation Testing". Except for occasional spikes representing the intrusions of oxide into the alloy, the TGO thickness is relatively uniform for all the baseline specimens.

Figure 7 shows the TGO thickness variation in form of a cumulative probability distribution (CPD) for the four baseline specimens. The black curve (single specimen baseline) depicts the distribution for the specimen which was oxidized alone. The other three curves (modified baselines – left, right, and center) represent the distributions of specimens from the modified baseline experiment. The single baseline specimen has a slightly higher average TGO thickness than the center modified baseline specimen, suggesting that the altered air flow due to the physical presence of the deposits has at most a modest effect on the oxidation behavior. There is more variation in the CPD depending on the specimen location in the furnace hot zone, with the left and right specimens exhibiting slightly lower average TGO thickness than the center specimen. To capture the expected range of experimental variation absent deposits, the portion of the TGO thickness distributions spanning from the 5% mark of the leftmost CPD curve to 95% of the rightmost CPD curve is defined as

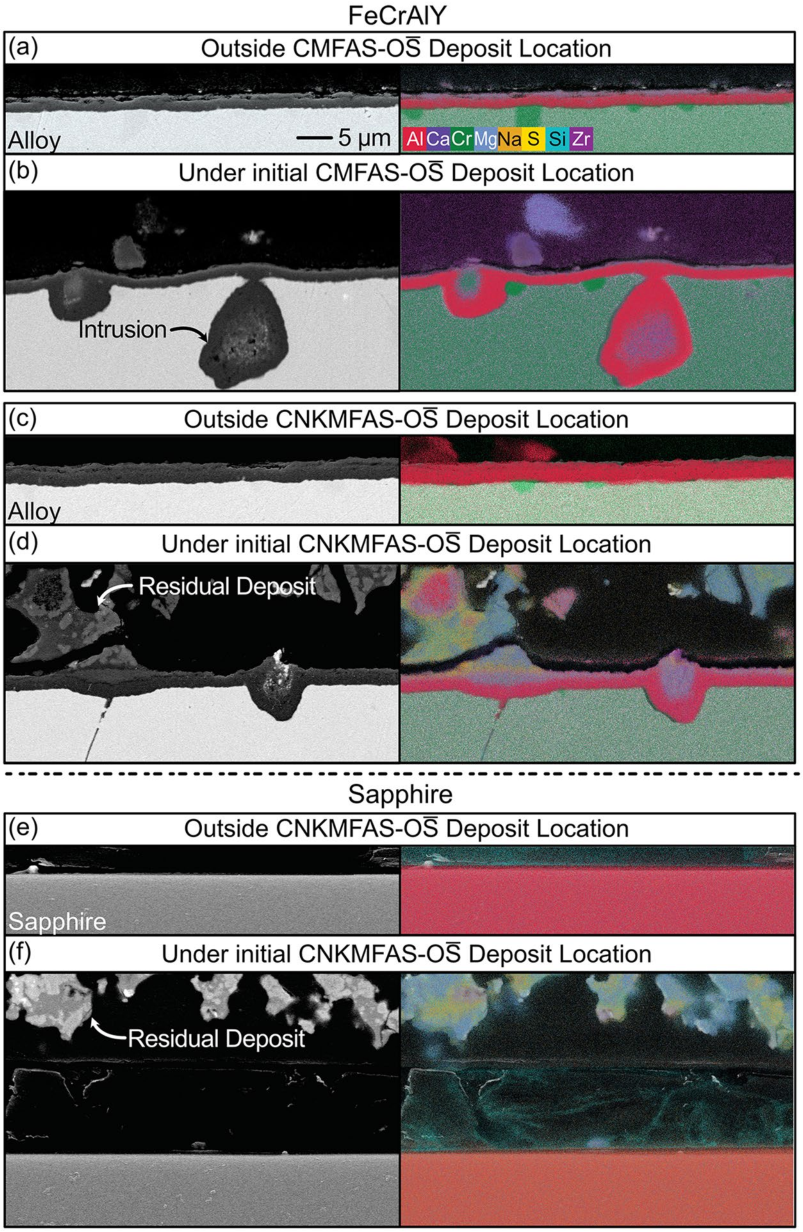

Fig. 5 Analysis of the corrosion products formed on the FeCrAlY alloy exposed to **a**, **b** CMFAS – O$\overline{S}$ and **c**, **d** CNKMFAS – O$\overline{S}$ deposits and on the sapphire specimen exposed to **e**, **f** CNKMFAS – O$\overline{S}$ deposit. The left column shows BSE images, and the right column shows EDS maps of key elements

the shaded 'baseline' region in the subsequent discussion. The CPD curves falling in this region for specimens exposed to the deposits would signify minimal corrosive effect of the deposits.

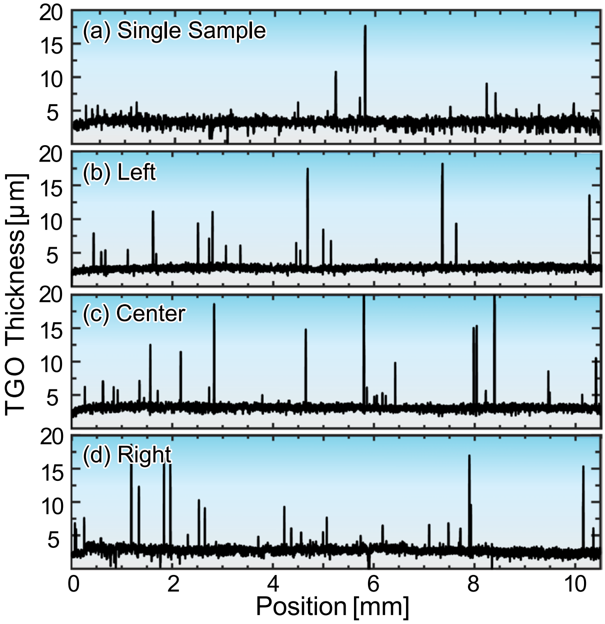

Fig. 6 Plots of the TGO + RP thickness as a function of position across the FeCrAlY specimen for the **a** single baseline specimen and for modified baseline specimens situated toward the **b** left, **c** center, and **d** right of the furnace hot zone, as defined in Fig. 7

Effect on the TGO + RP and RP Thicknesses

Figure 8 shows the TGO and TGO + RP thicknesses as a function of position across the cross sections for each FeCrAlY specimen and for the two sapphire specimens where reactions were evident. Except for occasional spikes representing the intrusions of oxide into the alloy, the TGO thickness is relatively uniform for the specimens exposed to the mixed oxides (Fig. 8a,b) and the mixed oxide–sulfate deposits (Fig. 8c,d). In comparison, the formation of calcium aluminates upon reaction with $CaSO_4$ roughly doubles the TGO + RP thickness in places where there was favorable contact between the deposit and the alloy (Fig. 8e). The reaction product layer formed under the $CaSO_4$ deposit on the sapphire is comparable in thickness to the increase in the TGO + RP thickness for FeCrAlY relative to the baseline. It is similarly sporadic, presumably due to varied contact with the powdered deposit, and isolated reactions outside the deposit are due to the scattering of the $CaSO_4$ particles (Fig. 8g). Figure 8f shows that the degradation of the Al_2O_3 TGO by the $\mathrm{CNKM}-\overline{\mathrm{S}}$ deposit, resulting in increased TGO + RP thickness and increased frequency and depth of intrusions into the alloy, was uniform across the entire specimen. Conversely, the attack of the sapphire by $\mathrm{CNKM}-\overline{\mathrm{S}}$ (Fig. 8h) was more concentrated in the center and diminished toward the periphery, possibly due to the depletion of reactants by the more vigorous initial reaction. A drop in the RP thickness at multiple locations suggests cracking and delamination of reaction products.

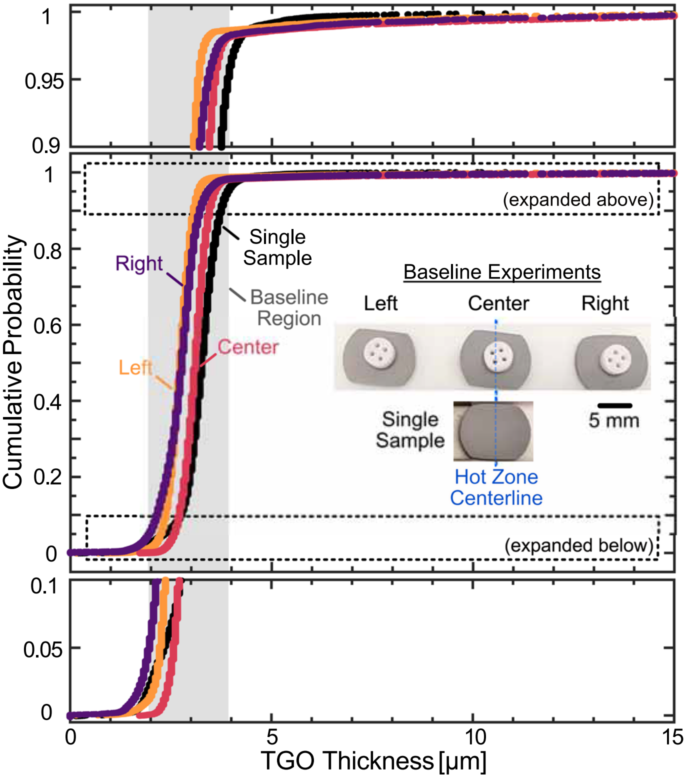

Fig. 7 Cumulative probability distribution (CPD) of the TGO thickness on the baseline specimens

A comparison of the panels in Fig. 8 shows that the primary difference in behavior for the specimens exposed to the mixed oxide and oxide–sulfate is the frequency of deeper oxide intrusions with the latter being much higher. To quantify this effect, the percentage of points in each region corresponding to either twice (2x) or thrice (3x) the average was calculated. The results are shown in Fig. 9. Even though reactions are evident on sapphire specimens exposed to sulfate deposits, no significant intrusions were observed. Hence, similar analysis was not performed for sapphire specimens.

The region outside mixed oxide, mixed oxide–sulfate, and $CaSO_4$ deposit locations showed two and three-fold intrusion percentages around 1% and 0.4%, respectively, roughly similar to the average baseline behavior. Except for CMFAS – O, the intrusions under other oxide and oxide–sulfate deposits increased at least by twofold compared to the region outside of the deposit. The increase in the frequency of oxide intrusions could either be attributed to a transient melt, favorable contact of unreacted sulfates, increased reactivity following the addition of Na and K salts, or just to the presence of deposits at the local defect locations causing the intrusions. These results also reinforce the conclusion

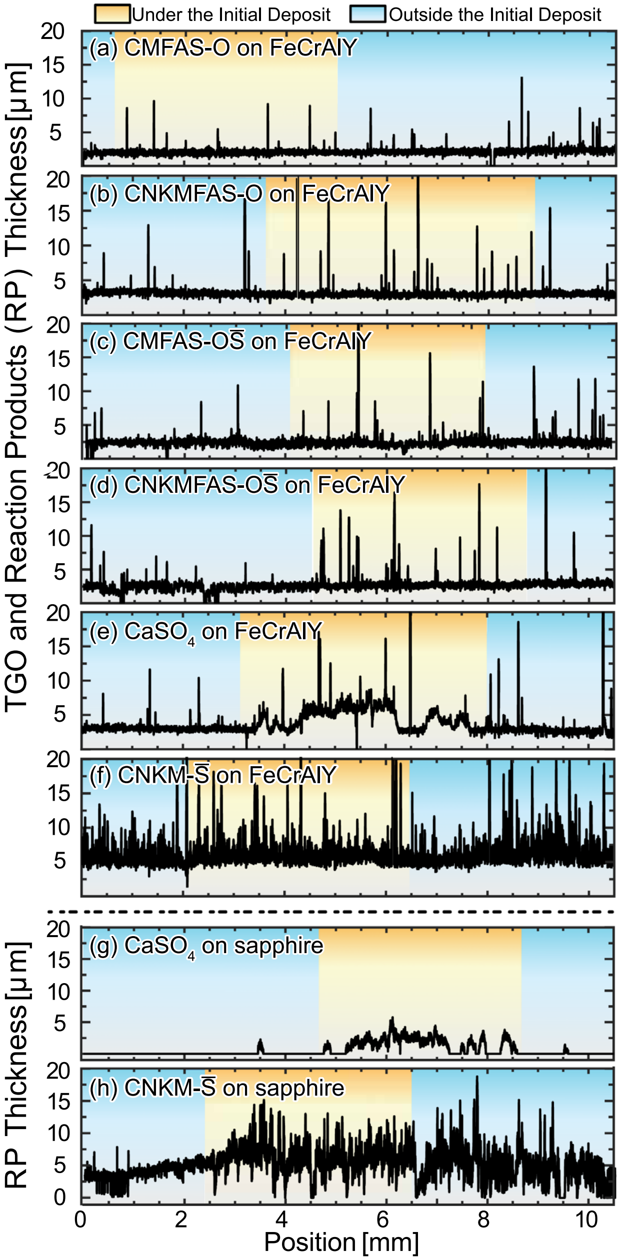

Fig. 8 Plots of the TGO + RP thickness as a function of position across the **a**-**f** FeCrAlY specimen after exposure to **a** CMFAS – O **b** CNKMFAS – O **c** CMFAS – O$\overline{S}$ **d** CNKMFAS – O$\overline{S}$ **e** CaSO$_4$ **f** CNKM – $\overline{S}$, and of RP thickness on sapphire specimens exposed to **g** CaSO$_4$ and **h** CNKM – $\overline{S}$ deposits at 1025 °C for 100 h

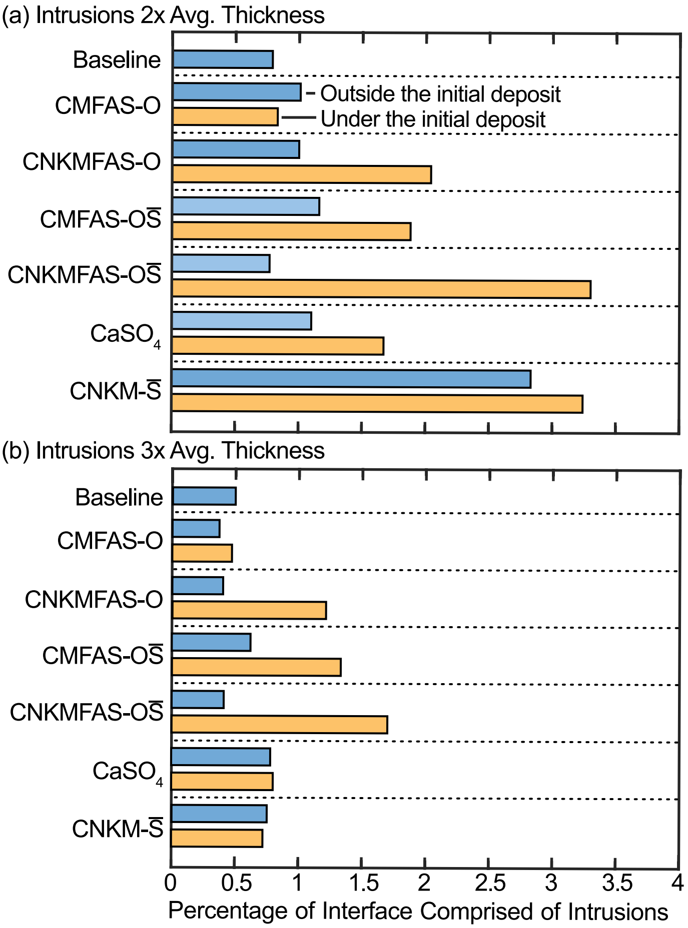

Fig. 9 The prevalence of oxide intrusions either **a** twice or **b** thrice the average TGO + RP thickness reported as a fraction of the cross section length of the specified region. Regions defined as under or outside the initial location of deposits are shown in Fig. 8

that the effect of oxide–sulfate deposits, if any exists, is highly localized. The percentage of 2 × intrusions under the $CaSO_4$ deposit increased by a factor of two compared to the baseline due to the formation of non-protective aluminates. The CNKM – $\overline{S}$ deposit increased the frequency of intrusions across the specimen by a factor of three to four compared to the baseline. The percentage of 3 × intrusions under both sulfate deposits, even though slightly higher than baseline, was lower compared to that under the mixed oxides, and oxide–sulfate deposits in part due to the increase in average TGO + RP thickness.

To assess the effect of deposits on accelerating the alloy oxidation (compared to simply consuming alumina), the sapphire RP thickness data were shifted by adding a thickness equivalent to the average α-Al_2O_3 growth observed on the corresponding FeCrAlY specimens. This shifted sapphire RP thickness represents an equivalent to

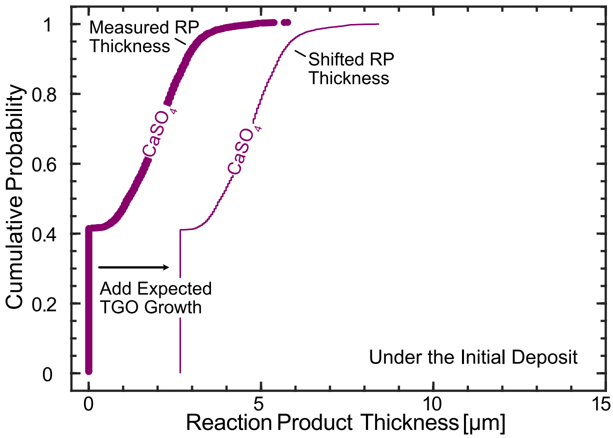

Fig. 10 CPD of the RP thickness and shifted RP thickness (after adding the average α-Al_2O_3 thickness to the RP thickness) on the sapphire under the initial $CaSO_4$ deposit location

the TGO + RP thickness on an alloy specimen. Cumulative probability distributions illustrating this shift for the specimen exposed to the $CaSO_4$ deposit are shown in Fig. 10.

Figure 11a,b depicts the distribution of the TGO + RP thickness in regions under and outside the initial deposit location for all the FeCrAlY specimens. Except for the specimen exposed to the CNKM $-\overline{S}$ deposit, the regions outside the initial deposit location exhibited narrow thickness distribution falling within the shaded baseline band. The spreading of the CNKM $-\overline{S}$ melt drives reactions away from the original deposit location, shifting the CPD toward a higher TGO + RP thickness value (Fig. 11a). The CPD for the regions under the mixed oxide and oxide–sulfate deposits also falls in the baseline band except for the longer tail at high TGO + RP thicknesses due to the increased frequency of the deep oxide intrusions (see Fig. 11b).

Owing to the uniform reaction of the CNKM-$\overline{S}$ deposit with the TGO throughout the deposit, the CPD behavior of the region under the initial deposit did not change significantly compared to the region outside the initial deposit location. The skewing of the curve at higher TGO + RP thickness values denotes the large fraction of deeper oxide intrusion in the alloy. The shape of the CPD for the region under the $CaSO_4$ deposit changes relative to the other specimens. The reaction of the $CaSO_4$ deposit with the TGO to form thicker calcium aluminates shifts the CPD compared to the region outside the initial deposit location. The shift for the CNKM-$\overline{S}$ deposit is larger than for $CaSO_4$ in part because the molten deposit accelerated the reaction with the TGO.

Figure 11c and d compares the CPD for the FeCrAlY to the modified CPD for sapphire exposed to $CaSO_4$ and CNKM $-\overline{S}$. The first 20% of the distribution for regions outside the initial CNKM $-\overline{S}$ deposit on sapphire falls to the left of (smaller RP thickness) FeCrAlY due to partial RP spallation on the sapphire. The remainder of the distributions are closely aligned. The CPD for the sapphire outside the $CaSO_4$ deposit location shows a sharp increase with only a small tail toward higher

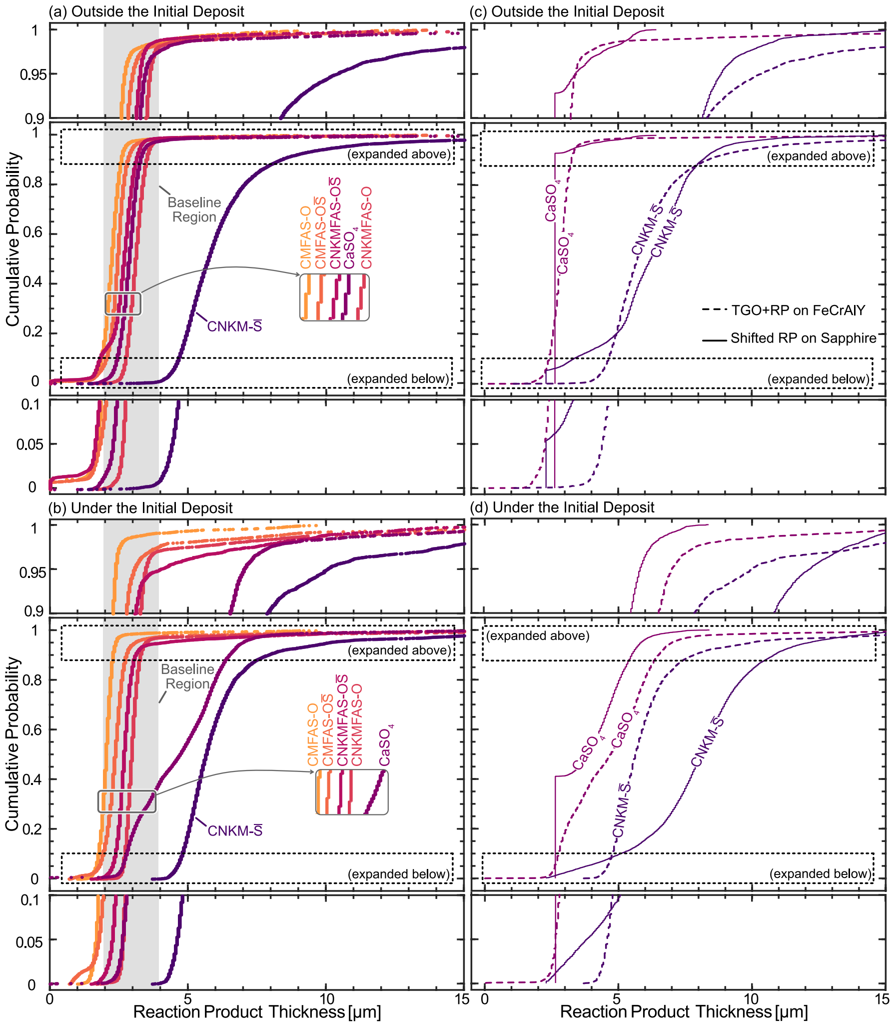

Fig. 11 CPD of the TGO + RP thickness **a**,**b** for all deposits on FeCrAlY and **c**,**d** comparison of FeCrAlY and the shifted sapphire data **a**,**c** outside and **b**,**d** under the initial deposit

RP thickness due to reaction with scattered $CaSO_4$. Approximately 40% of the area under the $CaSO_4$ deposit on sapphire doesn't show evidence of a reaction product, leading to the sharp jump at the start of the CPD in Fig. 11d. The FeCrAlY exhibits a similar steep rise, although normal variability in the TGO thickness spreads the distribution slightly. Thereafter, the two CPDs follow a similar trend but the CPD for the sapphire is shifted to the left of the CPD for the FeCrAlY, possibly due to a slight increase in the oxidation rate under the $CaSO_4$. Under the $\text{CNKM} - \overline{\text{S}}$ deposit on sapphire, there are some instances of reaction product cracking and delamination shifting the first 10% of the distribution to the left of the equivalent FeCrAlY distribution. Then the CPD for RP depth under $\text{CNKM} - \overline{\text{S}}$ on sapphire passes FeCrAlY toward a higher RP thickness value. This supports the hypothesis that the Al_2O_3 reservoir on the sapphire leads to greater dissolution initially when the deposit melts. These observations also suggest that the effect of the TGO reaction products to increase the oxidation rate is modest since most of the increase in TGO + RP thickness relative to the baseline can be attributed to the increase in volume as CaO is incorporated in the reaction products.

Effect on the Interface Roughness

Figure 12(a,b) shows the interface height CPD for the region outside and under the initial deposit location of each of the FeCrAlY specimens. In these plots, a shallower slope and wider distribution corresponds to increased interface roughness. The corresponding relative interface height plot as a function of location is provided in Supplementary Information – Appendix A. All the baseline specimens had a narrow distribution ranging from − 1.5 to 1.5 µm, indicating limited interface roughening and hence only a single representative baseline CPD is plotted. The regions outside the initial deposit locations have similarly narrow roughness distributions (Fig. 12a) except for $\mathrm{CNKM}-\overline{\mathrm{S}}$, which shows increased interface roughness due to reactions with the melt spreading outside the initial deposit location. The CPDs for the regions under the mixed oxide and oxide–sulfate deposits (Fig. 12b) are also similar to the baseline behavior. In comparison, the formation of aluminate products in reaction with the $CaSO_4$ and $\mathrm{CNKM}-\overline{\mathrm{S}}$ deposits increased the interface roughness, broadening the CPD.

Figure 12(c,d) shows the CPD for the reaction layer-sapphire interface positions. For equivalent deposits, the CPDs for the sapphire specimens are narrower than the FeCrAlY counterparts. The distribution for the baseline specimen, with approximately 98% of the distribution within ± 200 nm, indicates the minimum sensitivity of the specimen preparation and measurement technique. Apart from $\mathrm{CNKM}-\overline{\mathrm{S}}$, the CPD for regions outside the deposits is similar to the baseline behavior, with only slight differences due to occasional surface chipping during the metallographic preparation. Likewise, no change was evident under the $\mathrm{CNKMFAS}-\mathrm{O}$ and $\mathrm{CNKMFAS}-\mathrm{O}\overline{\mathrm{S}}$ deposits. Under the $CaSO_4$ and $\mathrm{CNKM}-\overline{\mathrm{S}}$ deposits, the interface roughness increased in comparison to the region outside the deposit (see Fig. 12d) leading to the broadening of the CPD curve. The extensive reaction of the sapphire via a fluxing mechanism under the $\mathrm{CNKM}\text{-}\overline{\mathrm{S}}$ deposit more significantly increases the interface roughness, further broadening the CPD curve (see Fig. 12d).

Implications for Deposit-Induced Degradation of Advanced Alloys

The results provide quantitative information about the effect of deposit composition on alloy hot corrosion and TGO reactions. The first objective of the study was to compare the corrosive effects of deposits developed from the mixtures of oxides and

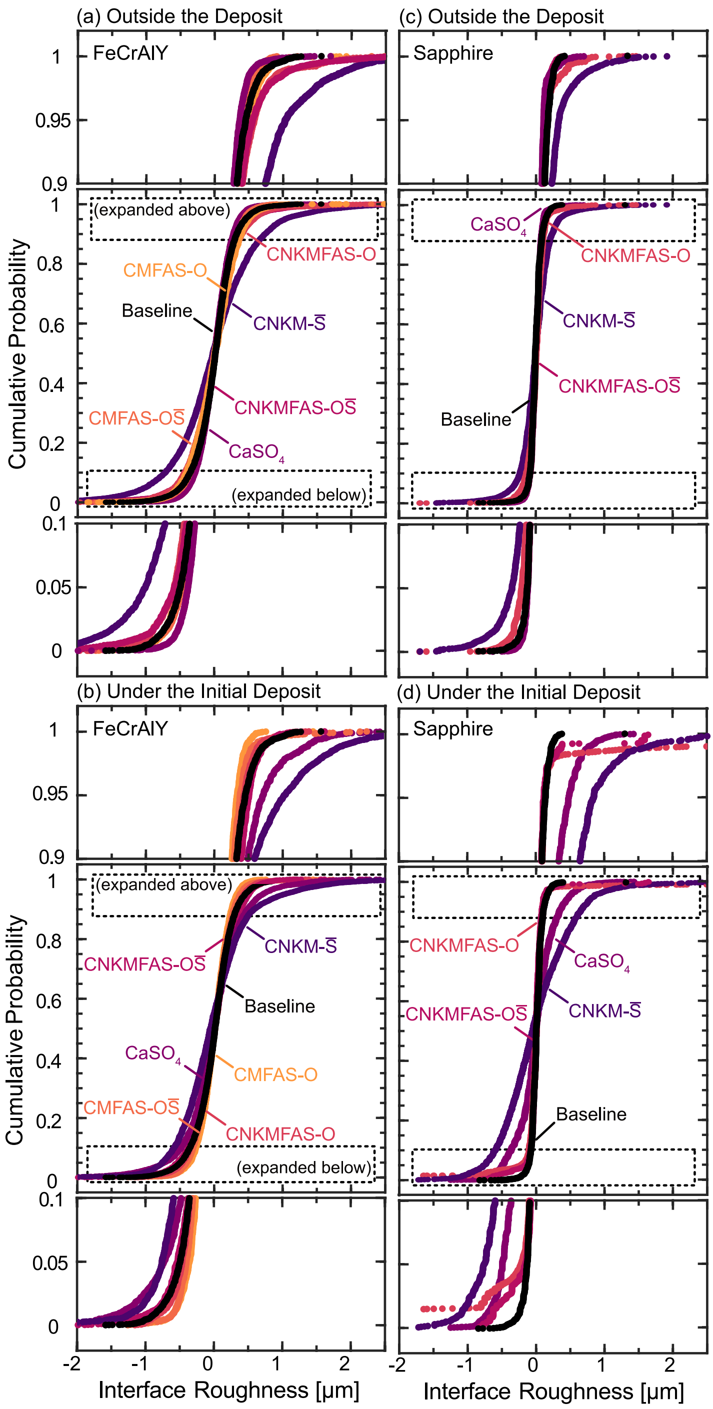

Fig. 12 CPD of the interface roughness **a**, **c** outside and **b**, **d** under the initial deposit position for the FeCrAlY and sapphire specimens

oxide–sulfate salts. The results show that because of the rapid decomposition of the sulfates in the oxide–sulfate deposits and the formation of stable silicate products, there was little difference between the oxides and oxide–sulfate deposits except for an increase in the frequency of TGO intrusions under the sulfate-containing deposits. This is true even for the Na-containing deposits where sodium silicate formation traps the Na adjacent to the alloy. The fact that intrusions were not observed on the sapphire specimens could imply that it was the combination of alloy composition, microstructure, and deposit contact that drove the attack rather than just the TGO-deposit reactions.

The second objective of the study was to compare the behavior of a solid ($CaSO_4$) deposit and a $CaSO_4$-based low-melting deposit ($\mathrm{CNKM}-\overline{\mathrm{S}}$). The results show that both the specimens formed thick, layered calcium aluminates with similar thickness distribution. The variation in the degree of contact between the deposit and the specimen surface affected the thickness of the reaction product layer. On the other hand, the presence of melt in the $\mathrm{CNKM}-\overline{\mathrm{S}}$ deposit led to the dissolution of the Al_2O_3 and subsequent reprecipitation of aluminate products. The results show that the sapphire formed thick and porous products whereas the reaction product layer on the alloy was thinner and denser. The implication is that the dissolution kinetics on both the specimens varied either due to the presence of a semi-infinite supply of Al_2O_3 on the sapphire as compared to the limited Al_2O_3 thickness on the alloy, or due to the presence of transient Cr and Fe oxides along with Al_2O_3 on the FeCrAlY alloy. On both the specimens, MgO was observed above the reaction layer primarily under the deposit and less often around the periphery of the reaction layer. This implies that the $MgSO_4$ decomposes during the heat treatment and does not participate in the reactions. The TGO + RP thickness distribution on both the specimens exposed to just sulfates suggests that the increase in the rate of oxidation due to the formation of aluminate reaction products is modest and the shift in TGO + RP thickness is majorly due to the incorporation of CaO into the TGO.

A final implication is that although tests on sapphire substrates can decouple the alloy effect from the TGO-deposit reactions to accelerate understanding of the effect of large sets of variables on the deposit-induced degradation process, the semi-infinite alumina changes the reactions in some cases, especially those involving transient melts.

Conclusions

Using a combination of local microstructure characterization and image analysis, this work improved the understanding of how oxide, oxide–sulfate, and sulfate deposits change the oxidation of FeCrAlY alloy and react with sapphire. Key conclusions are:

1. The frequency of oxide intrusions into the FeCrAlY increased under the deposits compared to the baseline specimens. This effect was more pronounced for deposits containing Na. Equivalent local reaction product intrusions were not observed on the sapphire specimens.
2. The corrosion behavior for the mixed oxide–sulfate deposits was similar to the initially sulfate-free mixed oxide deposits.
3. The $CaSO_4$ and $\mathrm{CNKM}-\overline{\mathrm{S}}$ deposits both formed layers comprising primarily calcium aluminate reaction products. The reaction layer under the $CaSO_4$ was less uniform than under the molten $\mathrm{CNKM}-\overline{\mathrm{S}}$ due to variations in the degree of contact between the solid $CaSO_4$ particles and the TGO or sapphire surfaces. The reaction layer was thicker under the initial $\mathrm{CNKM}-\overline{\mathrm{S}}$ deposit on sapphire, likely due to the fast initial dissolution reaction.
4. Analysis of the TGO and RP layer thicknesses suggests that although the effective TGO thickness increases on exposure to the sulfate deposits, this is due primarily to CaO incorporation in the TGO and that the aluminate products have a modest effect on increasing the oxidation rate.

Supplementary Information The online version contains supplementary material available at https://doi.org/10.1007/s11085-023-10182-2.

Acknowledgements The authors are grateful to Drs. Pin Lu, Changning Niu, and Jiadong Gong (QuesTek Innovations LLC) for the insightful discussions, and to Dr. Eeshani Godbole for assistance preparing the deposit powders.

Author Contributions Both authors designed the study. AC performed the experiments, characterization, and initial data analysis, prepared the figures, and wrote the first draft of the manuscript. DP contributed to data interpretation and edited the figures and manuscript. Both authors reviewed the final manuscript.

Funding This research was supported by the Office of Naval Research (Award number N68335-20-C-0472 monitored by Dr. David Shifler) in collaboration with QuesTek Innovations LLC. Part of this work was carried out in the Characterization Facility, College of Science and Engineering, University of Minnesota, which receives support from the National Science Foundation through the MRSEC (Award Number DMR-2011401) and the NNCI (Award Number ECCS-2025124) programs.

Declarations

Conflict of interest The authors declare that they have no conflict of interest.

References

1. P. Marcus, *Corrosion science.* **36**, 1994 (2155).
2. B. Gleeson, *Shreir's corrosion.* 182, (2010)
3. J. A. Goebel and F. S. Pettit, *Metallurgical Transactions.* **1**, 1970 (3421).
4. J. A. Goebel, F. S. Pettit, and G. W. Goward, *Metall Mater Trans B.* **4**, 1973 (261).
5. G. W. Goward, *Journal of Engineering for Gas Turbines and Power.* **108**, 1986 (421).
6. N. Eliaz, G. Shemesh, and R. M. Latanision, *Engineering Failure Analysis.* **9**, 2002 (31).
7. J. Stringer, *Annual Review of Materials Science.* **7**, 1977 (477).
8. R. A. Rapp, *Corrosion Science.* **44**, 2002 (209).

9. K. L. Luthra, *Reaction mechanism. Metallurgical Transactions A*. **13**, 1982 (1853).
10. K. L. Luthra and D. A. Shores, *Journal of the Electrochemical Society*. **127**, 1980 (2202).
11. R. L. Jones, Cobalt oxide-SO_2/SO_3 reactions in cobalt-sodium mixed sulfate formation and low temperature hot corrosion. in: *High temperature corrosion. Proceedings of the International Conference, San Diego, CA, March 2–6, 1981*. 1983.
12. K. Y. Jung, F. S. Pettit, and G. H. Meier, The effect of Ca-rich deposits on the high temperature degradation of coated and uncoated superalloys. in: *Materials Science Forum*. Trans Tech Publ; 2008.595:805–812.
13. T. Gheno, G. H. Meier, and B. Gleeson, *Oxidation of Metals* **84**, 2015 (185).
14. M. B. Krisak, B. I. Bentley, A. W. Phelps, and T. C. Radsick, *Journal of Propulsion and Power*. **33**, 2017 (697).
15. P. Brennan, Environmental Factors Affecting CaO-and $CaSO_4$-Induced Degradation of Second-Generation Nickel-Based Superalloys. University of Pittsburgh; 2020.
16. M. Kovalchuk, and B. Gleeson, Laboratory-Scale Replication of Deposit-Induced Degradation of High-Temperature Turbine Components. in: *Superalloys 2020*, eds. S. Tin, M. Hardy, J. Clews, et al. (Springer International Publishing; Cham, 2020). pp. 789–797. doi:https://doi.org/10.1007/978-3-030-51834-9_77.
17. A. S. Chikhalikar, E. P. Godbole, D. L. Poerschke *Corrosion Science*. 110892. (2022) doi:https://doi.org/10.1016/j.corsci.2022.110892
18. D. A. Shifler, The Increasing Complexity of Hot Corrosion. In: American Society of Mechanical Engineers Digital Collection; 2017. doi:https://doi.org/10.1115/GT2017-65281
19. D. A. Shifler, and S. R., Choi, CMAS Effects on Ship Gas-Turbine Components/Materials. In: *ASME Turbo Expo 2018: Turbomachinery Technical Conference and Exposition*. American Society of Mechanical Engineers Digital Collection; (2018)
20. D. A. Shifler, *Materials at High Temperatures*. **35**, 2018 (225).
21. K. J.Meisner, E. J. Opila, *Oxid Met*. 2020; doi:https://doi.org/10.1007/s11085-020-09990-7.
22. J. L. Smialek, F. A. Archer, and R. G. Garlick, *JOM* **46**, 1994 (39).
23. T. Gheno and B. Gleeson, *Oxidation of Metals*. **87**, 2017 (249).
24. T. Gheno and B. Gleeson, *Oxidation of Metals* **86**, 2016 (385).
25. D. L. Poerschke, R. W. Jackson, and C. G. Levi, *Annual Review of Materials Research*. **47**, 2017 (297).
26. C. G. Levi, J. W. Hutchinson, M.-H. Vidal-Sétif, and C. A. Johnson, *MRS bulletin*. **37**, 2012 (932).
27. A. R. Ericks, F. W. Zok, D. L. Poerschke, and C. G. Levi, *Journal of the American Ceramic Society*. **105**, 2022 (3665).
28. G. H. Meier, *Oxidation of Metals* **98**, 2022 (1).
29. A. S. Chikhalikar, E. P. Godbole, and D. L. Poerschke, *Acta Materialia* **237**, 2022 (118184).
30. P. T. Brennan, D. Konitzer, and M. Brennan, B Gleeson, *Oxidation of Metals*. 1 (2022)
31. W. D. Summers, D. L. Poerschke, D. Park, J. H. Shaw, F. W. Zok, and C. G. Levi, *Acta Materialia* **160**, 2018 (34).
32. W. D. Summers, D. L. Poerschke, A. A. Taylor, A. R. Ericks, C. G. Levi, and F. W. Zok, *Journal of the American Ceramic Society* **103**, 2020 (2919).
33. D. W. Green and R. H. Perry, *Perry's chemical engineers' handbook*. (McGraw-Hill Education; 2008)
34. N. Kanari, N.-E. Menad, E. Ostrosi, et al., *Metals*. **8**, 2018 (1084).
35. P. G. Coombs and Z. A. Munir, *Journal of thermal analysis*. **35**, 1989 (967).
36. V. K. Tolpygo and D. R. Clarke, *Surface and Coatings Technology*. **120–121**, 1999 (1).
37. V. K. Tolpygo and D. R. Clarke, *Materials at High Temperatures*. **17**, 2000 (59).
38. E. M. Levin, C. R. Robbins and H. F. McMurdie. *Phase Diagrams for Ceramists*. 181, (1964)
39. B. Hallstedl, *Journal of the American ceramic society*. **73**, 1990 (15).
40. H. Du, *Journal of phase equilibria*. **21**, 2000 (6).
41. D. Freyer, W. Voigt, and K. Köhnke, *European Journal of Solid State and Inorganic Chemistry*. **35**, 1998 (595).
42. M. N. Scheidema and P. Taskinen, *Industrial & engineering chemistry research*. **50**, 2011 (9550).
43. A. Dimyati, H. J. Penkalla, P. Untoro, D. Naumenko, W. J. Quadakkers, and J. Mayer, *International Journal of Materials Research*. **94**, 2022 (180).
44. T. Sand, A. Edgren, C. Geers, et al., *Oxidation of Metals* **95**, 2021 (221).
45. B. A. Pint, *Journal of the American Ceramic Society*. **86**, 2003 (686).